

# Model based precision structural measurements on barely resolved objects

D. BADDELEY\*<sup>†</sup>, Y. WEILAND\*, C. BATRAM\*, U. BIRK\*  
& C. CREMER\*<sup>‡</sup>§

\*Kirchhoff Institut für Physik, Universität Heidelberg, Im Neuenheimer Feld 227,  
D-69120 Heidelberg, Germany

<sup>†</sup>Department of Physiology, University of Auckland, Auckland, New Zealand

<sup>‡</sup>Institute for Pharmacy and Molecular Biotechnology, Universität Heidelberg, D-69120 Heidelberg,  
Germany

<sup>§</sup>The Jackson Laboratory, Bar Harbor, ME 04609, USA

**Key words.** Confocal microscopy, size estimation, model based analysis.

## Summary

A model based method for the accurate quantification of the 3D structure of fluorescently labelled cellular objects similar in size to the optical resolution limit is presented. This method is applied to both simulated confocal images of chromatin structures and to real confocal data obtained on a Fluorescence *in situ* Hybridization (FISH) labelled gene domain. The model assumes that the object is composed of a small number of discrete points which are convolved with the microscope point spread function to give the image. Fitting this model to image data results in a method to assess object structure which is accurate, shows a low bias, and does not require user intervention or the potentially subjective setting of a threshold.

## Introduction

Many interesting biological structures are of a size similar to or smaller than the resolution of current light microscopy techniques such as Confocal Laser Scanning Microscopy (CSLM). An example of one such structure is replication foci which have been shown in electron microscopy to have a size of around 110 nm (Koberna *et al.*, 2005). Gene regions labelled with probes obtained from bacterial artificial chromosomes (BACs) are somewhat larger, the 200 kbp region of the *small nuclear ribonucleoprotein polypeptide N (SNRPN)* gene domain we measure in this paper turning out to be around 350 nm. Threshold based methods applicable to well resolved structures such as whole nuclei or, at a pinch, chromosome territories fail dismally on smaller structures having a size less than approximately 5–10 times the conventional resolution.

This is based on the premise that, in the absence of additional information about the imaging process and/or object, the error in any measurement is equal to the resolution. A measurement of an object five times larger than the resolution limit would thus incur an error of approximately 20%. Even when an objective/automatic threshold procedure is used sizes will be systematically overestimated.

An improved imaging resolution can be obtained using methods such as electron microscopy, X-ray microscopy, near field techniques such as Scanning Nearfield Optical Microscopy (SNOM) and the emerging far field optical techniques such as 4Pi, Stimulated Emission Depletion (STED) microscopy (for reviews see Gustafsson, 1999; Hell, 2003) and Spectrally Assigned Localization Microscopy (SALM; Betzig *et al.*, 2006; Hess *et al.*, 2006). Structured illumination (SI) techniques such as Spatially Modulated Illumination (SMI) microscopy (Failla *et al.*, 2002) also enable structural measurements at a precision significantly better than that obtainable with conventional light microscopy (Reymann *et al.*, 2008). All these methods have their respective advantages and disadvantages, and it is probably fair to say that there will always be problems which lie at the edge of any given microscope's resolution.

The imaging process in a microscope can be mathematically described by the point spread function (PSF). The PSF is the image obtained from an infinitely small, or 'pointlike', object and is equivalent to the impulse response in systems theory. Using knowledge of the PSF it is possible to extract significantly more information from an image. One of the simplest methods in which PSF information can be used is to perform deconvolution prior to thresholding. This does not however remove the subjectivity or intrinsic bias associated with the use of a threshold, and introduces various deconvolution related complications (McNally *et al.*, 1999).

These may include artifact generation, the introduction of an additional, subjective, regularization parameter, and, if an iterative method is used, an unpredictable and position/object dependant final resolution which makes it difficult to estimate measurement error. A full discussion of the pros and cons of structural measurements after deconvolution is beyond the scope of this paper, nonetheless an improvement in accuracy by a factor of 1.5–2 over threshold based measurements before deconvolution is likely to be realistic for objects smaller than approximately 1  $\mu\text{m}$ .

Another approach is to fit a mathematical model to the raw image data which describes both object form and the effects of the imaging process. Possibly the easiest model based method is fitting a Gaussian. Although a Gaussian fit is commonly used for position determination (Qu *et al.*, 2004; Betzig *et al.*, 2006; Lemmer *et al.*, 2008), its application to size determination has been limited. When both object and PSF are also approximated as Gaussians the width of the object is easily obtained from the width of the fitted curve using the formula

$$FWHM_{\text{object}}^2 = FWHM_{\text{fit}}^2 - FWHM_{\text{PSF}}^2$$

derived from the convolution of two Gaussians where FWHM is the full width at half maximum. Using this technique it is possible to clearly distinguish between 100 and 200 nm fluorescent beads, both of which have a sub-resolution size, in 2D sections from confocal images (our unpublished data).

For objects which are somewhat larger ( $\sim 350\text{ nm} - 1\ \mu\text{m}$ ), the assumption of Gaussian object form no longer yields a good agreement with the image data. Objects in this size range no longer appear as diffraction limited spots and typically show some lateral structure. Applying a threshold to these objects still does not yield sensible results, particularly in the  $z$ -direction (due to the anisotropy of the PSF), or for volume measurements. In this paper, we present a model in which the object is assumed to consist of a small number of pointlike objects. Note that as the number of points is chosen to be small, no correspondence to the location of individual fluorophores is assumed. It is nonetheless possible to form a good approximation to arbitrary structures. This model allows 3D size and shape parameters to be extracted with a precision significantly higher than that obtainable with threshold based methods. To demonstrate the technique we present measurements on simulated structures, the size and shape of which is known, and on real biological data, namely confocal measurements of the FISH labelled *SNRPN* locus. *SNRPN* is a bicistronic imprinted gene that is located within the Prader-Willi and Angelman syndrome region on human chromosome 15q11-q13. The gene is transcribed exclusively from the paternally inherited chromosome and encodes the *SNURF* and *SmN* polypeptides as well as several non-coding RNAs. Loss of the paternal allele leads to the development of Prader-Willi syndrome, a distinct neurogenetic disorder (Buiting *et al.*, 1995; Horsthemke & Buiting, 2006; Kantor *et al.*, 2006).

## Materials and methods

### Cells

Human lymphocytes (in G0) from fresh peripheral blood were obtained from a healthy male donor, isolated in a Ficoll gradient (FicoLite<sup>®</sup>-H, Linaris GmbH, Germany) washed twice in 50% FCS (PAA Laboratories GmbH, Germany)/RPMI 1640 medium (Invitrogen GmbH, Germany) and utilized for slide preparation.

### Slide preparation

The preparation of 3D preserved, paraformaldehyde (PFA) fixed lymphocyte nuclei was done according to standard protocols (Solovei *et al.*, 2002). In short, lymphocytes were seeded onto poly-L-lysine (Sigma-Aldrich, Germany) coated slides and fixed in 4% PFA (Sigma-Aldrich, Germany) in  $0.3 \times \text{PBS}$ , after a brief incubation in  $0.3 \times \text{PBS}$  to prevent shrinkage. Permeabilization steps included treatment in 0.5% Triton X-100 (Merck, Germany) in PBS, 20% glycerol (J.T. Baker, Deventer, NL) in PBS, repeated freeze thawing in liquid nitrogen and incubation in 0.1 M HCl. Slides were subsequently stored in 50% formamide (Merck, Germany) in  $2 \times \text{SSC}$  (pH 7.0) at  $4^\circ\text{C}$  until usage. At all steps drying of the cells was avoided.

### Fluorescence in situ hybridization

The DNA probe for *SNRPN* (200 kb), labelled with Oregon green, was purchased from Qbiogene (Carlsbad, CA). Probe preparation was carried out according to the manufacturers protocol.

DNA was denatured in 70% formamide in  $2 \times \text{SSC}$  (pH 7.0) at  $72^\circ\text{C}$  for 3 min. To prevent drying of the cells, the previously denatured probe was immediately placed onto the slide, covered with a cover slip and sealed with rubber cement.

Hybridization was performed for 2 days in a humid chamber at  $37^\circ\text{C}$ . Post-hybridization washings were done in  $4 \times \text{SSC}$ /Tween 20 (Fluka Chemie GmbH, Germany) (0.2%) at  $42^\circ\text{C}$  and  $1 \times \text{SSC}$  at  $60^\circ\text{C}$ . Nuclear DNA was counterstained with TO-PRO-3 (Invitrogen GmbH, Germany), afterwards cells were mounted in Vectashield (Vector Laboratories Inc, Burlingame, CA).

### Microscopy

Image acquisition was carried out with a Leica TCS NT Confocal Laser Scanning Microscope (CLSM) equipped with a PlanApo 63 $\times$ , NA = 1.4 oil immersion objective and an argon-krypton mixed gas laser for excitation at 488 nm and 647 nm. The excitation wavelengths were selected by an acousto optical tunable filter. The image size was  $512 \times 512$  pixels with voxel sizes of 78 nm in  $x$ - and  $y$ -direction and 203 nm in  $z$ -direction. The pinhole size was chosen to be equivalent to 0.7 Airy discs. To reduce noise, every section was accumulated

four times, corresponding to a total per pixel integration time of  $\sim 24$  ms.

### Simulation

'*In silico*' gene structures were created by modelling 200 kpb of chromatin as a 30 nm diameter fibre using the wormlike chain model (Kratky & Porod, 1949) and values for the persistence length and unit length of 150 nm and 10 nm/kpb, respectively (Munkel & Langowski, 1998). This resulted in a total length of 2  $\mu\text{m}$  which was divided into segments of length 10 nm for the computations. The wormlike chain model was implemented in Matlab (The Mathworks Inc., Natwick, MA) by choosing the bend,  $\theta$  and rotation,  $\phi$ , angles between segments from a random distribution. The segments were allowed to freely rotate –  $\phi$  was thus drawn from a uniform distribution covering the range  $[0, 2\pi)$ . Bending was however constrained, with  $\theta$  drawn from a Gaussian distribution of mean zero and with a standard deviation chosen such that the expectation value of  $\cos(\theta)$  followed the relationship  $\langle \cos(\theta) \rangle = e^{-s/l}$  where  $l$  is the persistence length and  $s$  the segment length, according to the definition of a wormlike chain. For the segment lengths and persistence lengths used, this corresponds to a mean angle of 16.7 degrees. A typical gene domain structure as generated using this model is shown in Fig. 1.

To obtain images from these model structures, virtual *fluorophores* were randomly distributed within a cylinder of radius 15 nm surrounding the fibre backbone. Five fluorophores were assumed in every 10 nm segment resulting in a total fluorophore number of 1000 for a 200 kpb gene locus. The images were then convolved with a theoretical confocal PSF, albeit using a NA of 1.25 in order to come closer to the performance typically observed in biological specimens, and subjected to a Poisson noise process assuming 10 counts per fluorophore (total of 10 000 counts in entire 3D image) and 2 counts of background. It is unclear whether, and

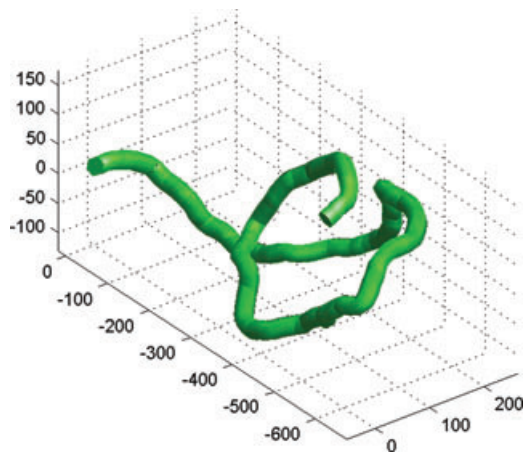


Fig. 1. Typical gene structure as simulated using the 30 nm fibre wormlike chain model. The axes are in nm.

probably even unlikely that, the number of fluorophores and the assumed counts per fluorophore are realistic. The values were chosen to ensure good coverage of the structure and to give a noise level similar to that observed in real images.

### Multi-point model

From the assumption that we can approximate the object by a small number of discrete points, it follows that the image will be the sum of the same number of PSFs, translated to the locations of the points and weighted with the point intensities. This gives the expression

$$I(\mathbf{r}) = \sum_i A \cdot I_{\text{PSF}}(\mathbf{r} - \mathbf{s}_i) \quad (1)$$

for the observed image intensity,  $I(\mathbf{r})$ , in which  $A$  is proportional to the intensity of a single point,  $\mathbf{s}_i$  the position of the  $i$ th point,  $I_{\text{PSF}}(\mathbf{r})$  the PSF, and  $\mathbf{r}$  the position in the resulting image.

In order to fit this model to the image we need a functional description of the PSF. This function should however be computationally inexpensive as it will typically be evaluated thousands of times during a fit. For confocal measurements the PSF can be reasonably approximated with a 3D Gaussian, which allows a reasonable computation time. The model is thus:

$$I(x, y, z) = A \sum_i e^{-\frac{x_i^2}{2\sigma_{xy}^2} - \frac{y_i^2}{2\sigma_{xy}^2} - \frac{z_i^2}{2\sigma_z^2}} + c \quad (2)$$

with  $\sigma_{xy}$  and  $\sigma_z$  chosen to give sensible lateral and axial FWHMs. The normalization contained in the factor  $A$ , a constant offset  $c$ , and the positions of the individual points ( $x_i, y_i, z_i$ ) are thus the free parameters in the fit. The values for  $\sigma_{xy}$  and  $\sigma_z$  should ideally be determined using calibration objects (e.g. fluorescent beads) in the same optical conditions as the objects to be measured. An optimum calibration would thus require, for example, the injection of calibration beads into cell nuclei. The empirical FWHM values of 250 and 600 nm for the lateral and axial directions, respectively, for a typical confocal microscopy measurement when using 488 nm excitation, however yield quite satisfactory results.

The number of points to take is a compromise between several factors including final accuracy, noise sensitivity, sensitivity to PSF approximations, convergence and speed. The greater the number of points, the better the model can represent an arbitrary object. A large number of points however makes convergence slow and increases the sensitivity to noise and errors in the PSF approximation. For the gene structures observed here, 10 points is sufficient to provide a good agreement between the original images and the model fit, and is used in the results throughout this paper. A schematic of the fit using 10 points to simulated gene-loci data is shown in Fig. 2.

If the number of fitted points was extended to infinity (practically the number of voxels in the image), the possible

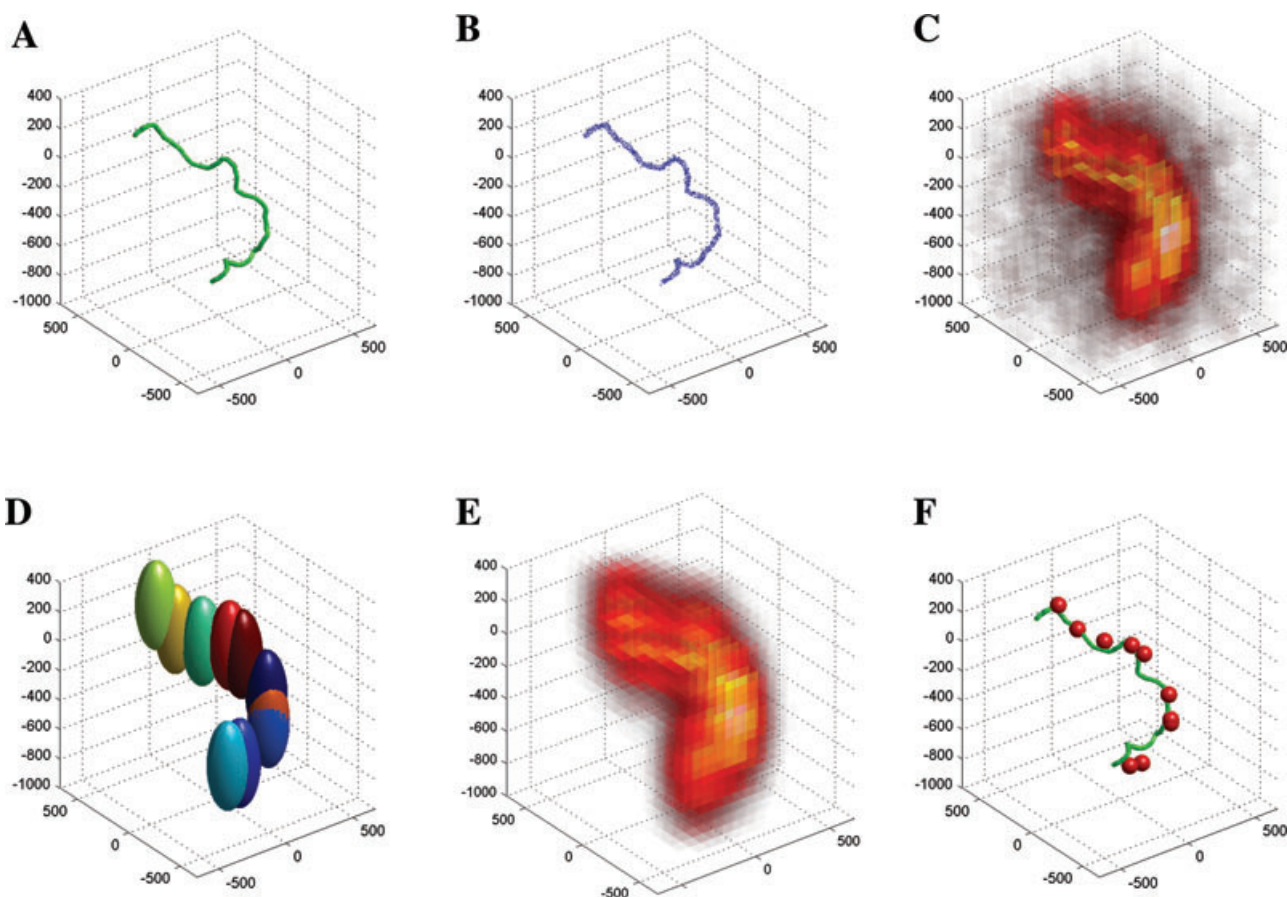


**Fig. 2.** Schematic diagram of the computer simulations used to generate the virtual gene foci images, and of the analysis procedure using the 10 point model. A gene loci structure is simulated as a random walk of 30 nm fibre (A). 1000 *virtual fluorophores* are randomly distributed within the volume of the fibre (B). A copy of a theoretical confocal PSF is placed at the location of each fluorophore to produce a 3D image stack which is then exposed to a Poisson noise process corresponding to 10 counts per fluorophore to give us our final *raw image data* (volume rendering: C). The data analysis consists fitting the model function in which the positions of 10 gaussian approximations to the PSF (D) are adjusted to produce the best match (volume rendering: E) to the raw image data. The centre of each of these points provides a good approximation to the underlying object structure (F). The scale in all images is in nm, the size of the voxels in the simulated data is  $78 \times 78 \times 200$  nm.

point positions restricted to a integer number of voxels, and the intensity of the individual points allowed to vary arbitrarily, then the fit would be equivalent to a maximum likelihood (ML) deconvolution. In restricting the number of points and enforcing equal point amplitudes, however, we strongly constrain the inverse problem. This improves the conditioning, and effectively allows *superresolution* measurements. The choice of suitable regularization techniques and constraints (e.g. positivity, minimum I-divergence, etc.) can serve a similar purpose, albeit to a lesser degree, in ML deconvolution. Allowing the point positions to take arbitrary values allows intrinsic sub-voxel accuracy, a feature not present in a deconvolution based approach (sub-voxel accuracy for certain types of measurements on deconvolved images is, at least in theory, possible).

In comparison to deconvolution, our fit based method benefits from its tighter constraints, allowing a higher

measurement accuracy for a small number of structural parameters. This improved accuracy is bought at the expense of the ability to represent all aspects of arbitrary structures.

The result of the fit is the position of each of the 10 points ( $x_i, y_i, z_i$ ) used in the model. In order to render this structural information in a form in which it is readily interpretable, further processing is required. A measure of the spread along each of the image axes can be obtained by taking the standard deviation of the appropriate position values. To allow an easy comparison with conventional *size* parameters we have converted the standard deviations into the FWHM of a corresponding Gaussian distribution by multiplying with  $2\sqrt{2 \ln(2)} \approx 2.355$  (this scale factor is obtained by setting  $\frac{1}{2} = \exp\left(-\frac{x^2}{2\sigma^2}\right)$ , taking the log of both sides, and solving for  $2x$ , the distance between the half height points).

The spread in one direction is only a good measure of object size when the object is rotationally symmetric. One possibility

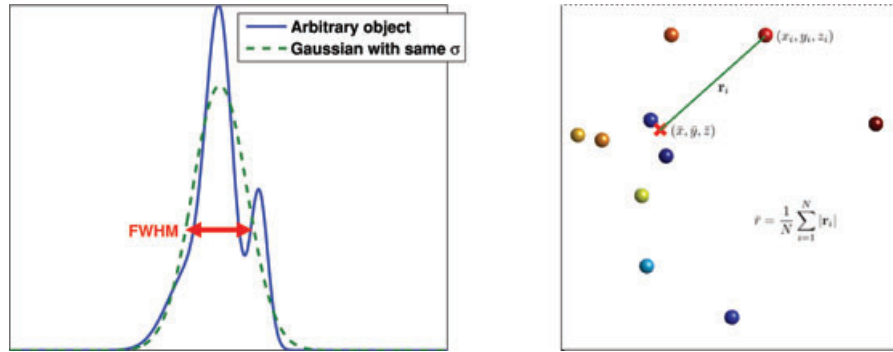


**Fig. 3.** Left-hand panel: Meaning of FWHM used in this paper for arbitrary objects: Due to the bimodality in the distribution shown it is unclear how to define a FWHM, for non-Gaussian distributions the true FWHM is also potentially a poor measure of spread. Our measured 'FWHM' values are thus calculated for a Gaussian distribution with the same standard deviation as the object. Right-hand panel: For 2 and 3D measurements we have taken the mean distance to the object centre as our size parameter and likewise transformed this parameter into the FWHM of a matching Gaussian.

for obtaining a 3D measure of object size is to take the mean of the three individual axes spreads. Standard deviation based measures are however quite sensitive to outlying points. We have thus chosen to base our size estimates on the mean distance from the object centre  $(x_c, y_c, z_c)$  to each of the points  $(x_i, y_i, z_i)$ , the object centre being calculated as the mean position of all 10 points. To calculate the extent along a given coordinate (e.g.  $x$ ), the mean distances were determined. The 2D extent was calculated as the mean distance  $\bar{r} = 1/N \sum_{i=0}^N \sqrt{(x_i - x_c)^2 + (y_i - y_c)^2}$ . As the resolution in the  $z$ -direction is worse than in the  $x - y$  plane, a 2D measure could be more accurate in some circumstances. As with the single axis spreads, we have converted our mean distance measure to a FWHM to allow easier comparison to conventional size measures. An overview of the size measures we used is shown in Fig. 3.

In addition to size, it is also possible to extract parameters describing object shape from the fit results. One such parameter is the anisotropy, calculated by determining the principle axes of the point distribution, projecting the point positions onto this axes system, and recalculating spread. The anisotropy can then be defined as the ratio between the spread along the major and minor axes. To keep it simple, and to avoid possible problems caused by the asymmetric resolution, the anisotropy measurements presented here have been restricted to the  $x$ - $y$  plane.

#### Data evaluation

Data evaluation was performed in Matlab, using a Levenberg–Marquardt non-linear fit to the model detailed above. In addition to the model based method, automatic thresholding (using the isodata algorithm) and measurements on the segmented data was performed using the DipImage toolkit (<http://www.ph.tn.tudelft.nl/DIplib/>).

## RESULTS

#### Model based fits to simulated 200 kbp gene regions

The computed images of 50 virtual gene structures were evaluated using the model based fit with 10 points (see also Fig. 2). A gallery of mean projections (average of all  $z$ -slices) of simulated images and their corresponding fits is shown in Fig. 4. It can be seen that the model is capable of providing a good approximation to the image data.

Figure 5 shows the relationship between  $x$  extent as calculated from the 'fluorophore' positions and that obtained when the model is fitted to the virtual images. In both cases the method of calculating extents illustrated in Fig. 3 was used. For comparison the results obtained using an automatic threshold algorithm are also shown. Results along the  $z$ -axis, having the worst optical resolution, are shown in Fig. 6. Although the model based technique produces a good estimate of object extent, measurements performed with a conventional threshold based algorithm show a strong bias, resulting in a systematic overestimation of object size (by as much as 800 nm in the  $z$ -direction) and a significantly higher variability. The small bias ( $x$ : 44 nm,  $z$ : 93 nm) present in the model based results can be attributed to an error in the estimate of the PSF size.

#### Fluorescent beads

Confocal images of various different sizes of fluorescent beads were performed to test the method on a real object of known size. The result of these measurements is shown in Fig. 7. In general the measured distributions are tight, indicating a high reproducibility, and in good agreement with the theoretical prediction. The larger spread of the 200nm diameter beads can be attributed to two factors; comparatively poor signal levels,

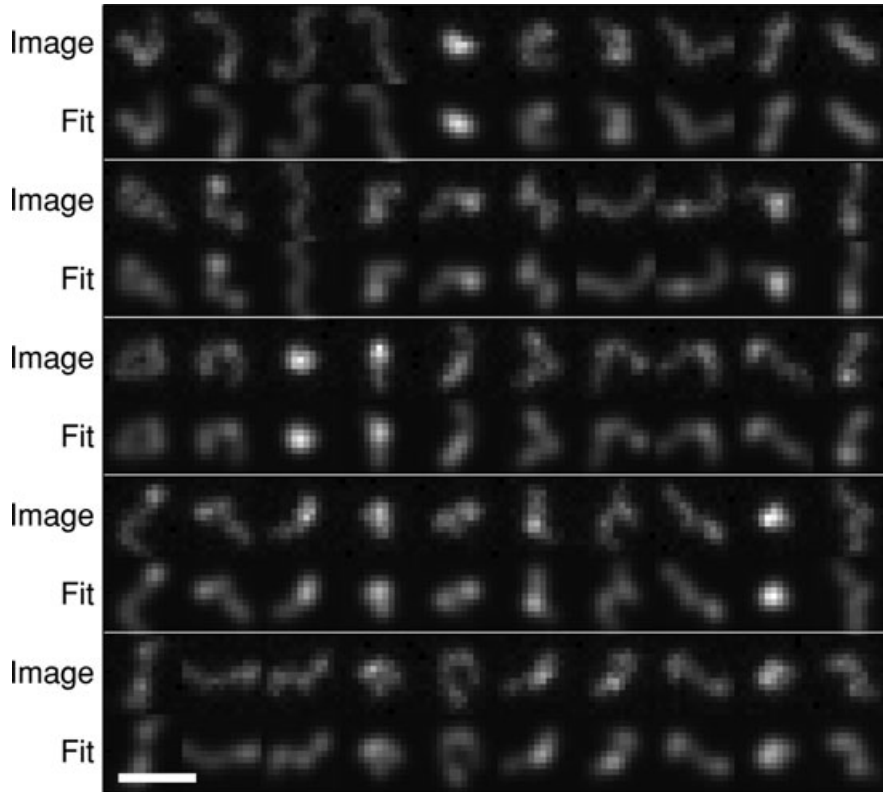


Fig. 4. Mean projections of 50 simulated confocal images of a 200 kbp 30 nm fibre segment and the accompanying 10 point fits. The scale bar is 1  $\mu\text{m}$ .

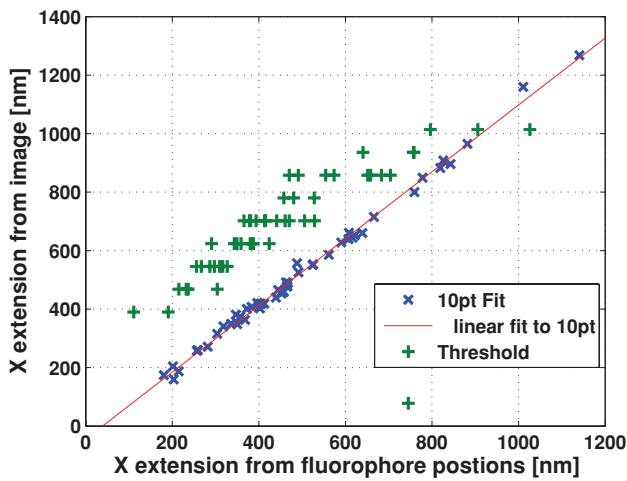


Fig. 5. Estimate of  $x$  extension from simulated image data compared with that extracted from the positions of the simulated fluorophores. The line of best fit to the model based extensions has the equation  $y = 1.1x - 44$ . In addition to the significant overestimation and larger spread the threshold based measurements also show quantization due to the finite voxel size.

and the presence of a small number of clusters containing more than one bead. The slight underestimation of the larger sizes can be attributed to the use of an approximate PSF, whose size was deliberately chosen to be slightly larger than that

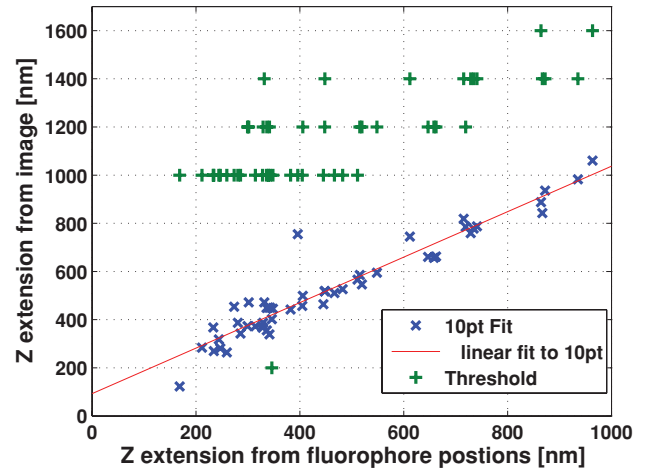


Fig. 6. Estimate of  $z$  extension from simulated image data compared with that extracted from the positions of the simulated fluorophores. The line of best fit to the model based extensions has the equation  $y = 0.94x + 93$ .

achievable in perfect optical conditions to better reflect the conditions found within cells.

*Model based fits to experimental data: the SNRPN locus*

Experimental confocal images of the SNRPN locus in 59 lymphocyte cell nuclei were made and evaluated using the

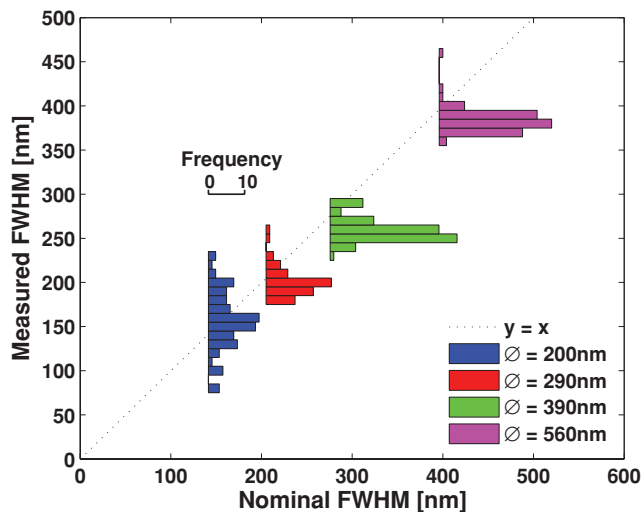


Fig. 7. Size distributions of various fluorescent beads measured using the 10 point model, showing a low variation and a good agreement with the manufacturers nominally stated sizes. Note that a factor of  $\sqrt{2}$  is required when converting between the diameter of a bead and its equivalent FWHM.

model based approach. A gallery of typical mean projection images and the mean projections of the corresponding fits is shown in Fig. 8. A good agreement is seen between the images and the fits. When compared with the simulated structures in Fig. 4 it is notable that the highly extended structures produced by the simulation are not observed in the experimental data. As the  $z$ -component of the point positions is the least accurate, we have limited our analysis to extension in the  $x$ - $y$  plane. Another, and equally compelling, reason for disregarding the  $z$  information principally contained within the 3D positions obtained from the fit is the effects introduced by sample refractive index. Refractive index mismatch and cell induced aberrations will broaden the effective PSF, thus effecting the accuracy of the measurements (Hell *et al.*, 1993). Although relatively small in the lateral directions, this broadening is quite pronounced along the optical axis. For future experiments requiring the reliable use of the  $z$ -axis information calibration objects within or on the surface of the cells would thus be desirable. The mean measured 2D extent of the SNRPN locus was  $346 \pm 51$  nm (*S.D.*).

The distribution of 2D extents is shown in Fig. 9 along with the distribution obtained from 5000 simulated gene structures generated under the assumption of a random polymer folding

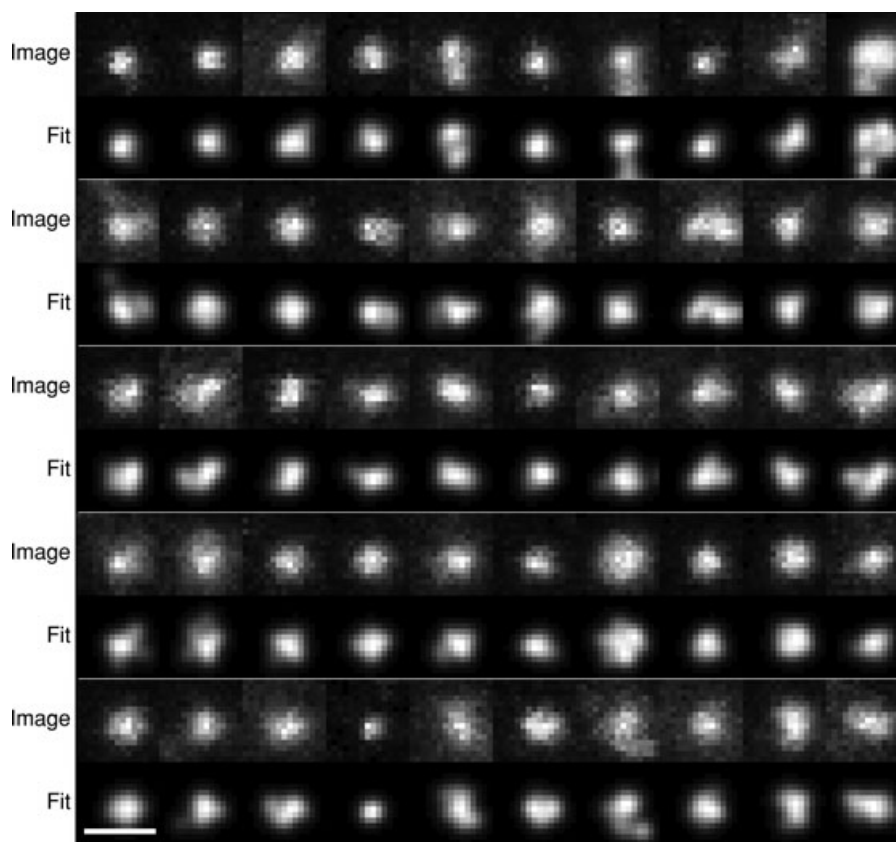


Fig. 8. Selection of typical experimentally obtained SNRPN loci images and their corresponding fits. Shown in each case is a mean projection of the original confocal image data, and a mean projection of the corresponding fit. The scale bar is 1  $\mu$ m.

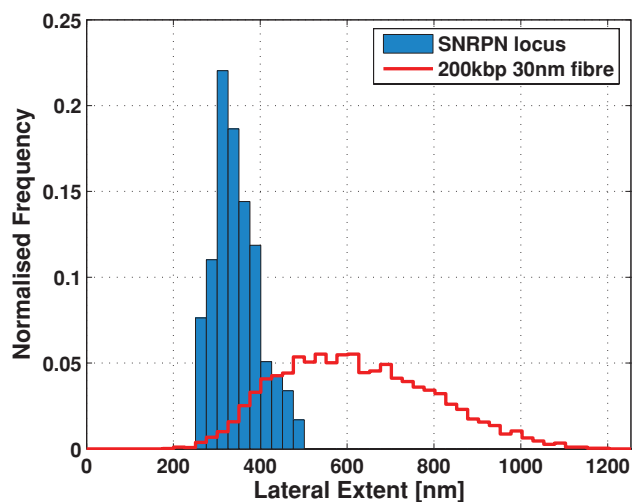


Fig. 9. Distribution of experimental *SNRPN* loci sizes labelled with a 200 kbp BAC probe. Shown for comparison is a numerically obtained distribution for 200 kbp of unconstrained 30 nm fibre. This empirical distribution was obtained by simulating 5000 configurations using the wormlike chain model and treating the segment positions in the same way the fitted point positions were treated.

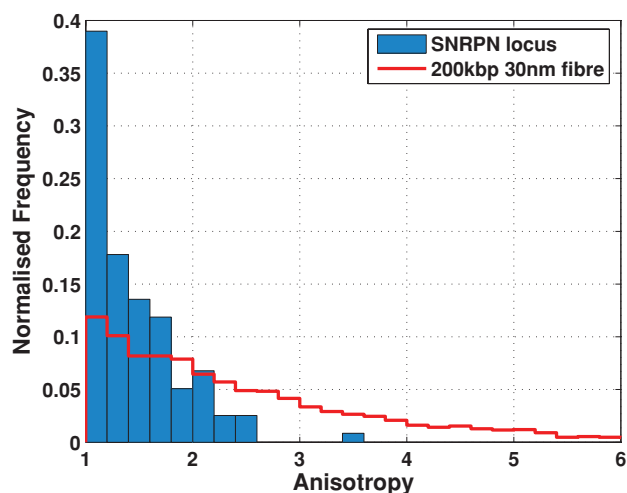


Fig. 10. Lateral anisotropy of the experimentally measured *SNRPN* loci, compared with a simulated distribution obtained from the wormlike chain model.

of 30 nm fibre (see Section ‘Materials and methods’). The extents of the simulated loci are in this case computed from the raw segment positions, not images. Although both distributions start at a lateral extent of approximately 230 nm, the measured distribution is significantly narrower, potentially indicating the presence of higher order chromatin structure. This is also suggested by the significantly lower anisotropy observed in the measured structures (see Fig. 10), which implies a tighter, more compact structure.

The *SNRPN* gene is located on chromosome 15q11.2, with the maternal allele being inactivated through imprinting. One might thus hypothesize a difference in the chromatin structure between alleles (Cremer & Cremer, 2001). The measured size distribution does not however appear to be bimodal. This does not rule out a difference, but does place limits on the size of such a difference, should it be present. Our results indicate that any difference in the sizes of the loci is less than around 100 nm, or a third of the locus size. This estimate is compatible with measurements performed using Spectral Precision Distance Microscopy (SPDM; Rauch *et al.*, 2008). In order to investigate the changes in more detail, one would need to identify either the imprinted or active locus through use of a cell line which allows the maternal and paternal alleles to be distinguished or techniques such as RNA FISH.

## Discussion

We have presented a model based method for extracting structural parameters from barely resolved images and demonstrated its application to confocal microscopy. The method exhibits significantly better accuracy than threshold based methods, and is also free from the subjectivity and effects of human intervention which plague threshold based techniques. Application to simulated images has shown the method to work, and measurements of the *SNRPN* locus in normal human lymphocyte nuclei show a compaction significantly greater than can be accounted for by a random folding of the 30 nm fibre alone.

The method as presented here uses a Gaussian approximation to the microscope PSF. Although this is a relatively good approximation one could contemplate the use of a more accurate model. The requirement for a functional representation of the PSF could potentially be avoided by interpolating on the fly between pixels of a sampled or experimental PSF, although this is likely to introduce a considerable performance hit (preliminary experiments indicate a factor of approximately 10 over a Gaussian approximation). Interpolation would be necessary in order to obtain sub-pixel accuracy and, more importantly, because the potential surface of the optimization function would otherwise take a staircase like form with large areas of zero gradient with jumps at multiples of the voxel size. The performance of any gradient descent algorithm on such a surface is doomed to be unimpressive. The method can easily be generalized to other microscope techniques such as widefield, SMI, 4Pi, or STED simply by introducing an appropriate functional approximation to the PSF.

Revisiting the compaction results, there is already a large base of evidence pointing to a higher order structuring of chromatin (Cremer & Cremer, 2001; O'Brien *et al.*, 2003; Horowitz-Scherer & Woodcock, 2006; Verschure, 2006). There are several mechanisms which could account for the additional compaction over and above that provided

by the 30 nm fibre, for example rosette formation. Recent computer models have attempted to model rosette formation through the introduction of mutually attractive segments into the 30 nm fibre (Odenheimer *et al.*, 2005). Such models could provide a better fit to our experimental data. Another explanation for the more compact foci sizes is some form of steric hindrance or crowding from the remainder of the nuclear contents. Although our results imply a significant amount of higher order compaction, it is difficult to draw any conclusions on the underlying form of the chromatin. Our results would be consistent with a 30 nm fibre exposed to some form of higher order compaction, although they do not rule out other possibilities. To fully investigate the underlying chromatin structure, and the potential changes therein, a more comprehensive study would be required with different sizes of genes in different states of activity.

The analysis of the size/structure of gene regions, as presented here, is only one potential application of the technique, which should be generally applicable to any barely resolved structures, in any type of imaging system. The FWHM measurement and the way in which it is extracted from the point positions is however particularly suited to compaction measurements. It is possible to extract other parameters (e.g. maximum distance to object centre/between two points) from the fitted positions, and conceivable that such an alternative measure may be more appropriate for certain questions. Although we would not recommend fitting the multi-point model to the reconstructed images produced by super-resolving single molecule techniques such as PALM, methods of size and shape determination analogous to the *mean distance from centre* and *anisotropy* measurements presented here could easily be applied to the unreconstructed fluorophore position data.

## Acknowledgements

We would like to thank the Deutsche Forschungsgemeinschaft (SPP 1128) and the European Union ('3D Genome' project) for funding.

## References

- Betzig, E., Patterson, G., Sougrat, R., *et al.* (2006) Imaging intracellular fluorescent proteins at nanometer resolution. *Science* **313**, 1642–1645.
- Buiting, K., Saitoh, S., Gross, S., Dittrich, B., Schwartz, S., Nicholls, R. & Horsthemke, B. (1995) Inherited microdeletions in the Angelman and Prader-Willi syndromes define an imprinting centre on human chromosome 15. *Nat. Genet.* **9**, 395–400.
- Cremer, T. & Cremer, C. (2001) Chromosome territories, nuclear architecture and gene regulation in mammalian cells. *Nat. Rev. Genet.* **2**, 292–301.
- Faila, A., Spoeri, U., Albrecht, B., Kroll, A. & Cremer, C. (2002) Nanosizing of fluorescent objects by spatially modulated illumination microscopy. *Appl. Opt.* **41**, 7275–7283.
- Gustafsson, M. (1999) Extended resolution fluorescence microscopy. *Curr. Opin. Struct. Biol.* **9**, 627–628.
- Hell, S. (2003) Toward fluorescence nanoscopy. *Nat. Biotechnol.* **21**, 1347–1355.
- Hell, S., Reiner, G., Cremer, C. & Stelzer, E. (1993) Aberrations in confocal fluorescence microscopy induced by mismatches in refractive index. *J. Microsc.* **169**, 391–405.
- Hess, S., Girirajan, T. & Mason, M. (2006) Ultra-high resolution imaging by fluorescence photoactivation localization microscopy. *Biophys. J.* **91**, 4258–4272.
- Horowitz-Scherer, R. & Woodcock, C. (2006) Organization of interphase chromatin. *Chromosoma* **115**, 1–14.
- Horsthemke, B. & Buiting, K. (2006) Imprinting defects on human chromosome 15. *Cytogenet. Genome Res.* **113**, 292–299.
- Kantor, B., Shemer, R. & Razin, A. (2006) The Prader-Willi/Angelman imprinted domain and its control center. *Cytogenet. Genome Res.* **113**, 300–305.
- Koberna, K., Ligasova, A., Malinsky, J., *et al.* (2005) Electron microscopy of DNA replication in 3-D: evidence for similar-sized replication foci throughout S-phase. *J. Cell. Biochem.* **94**, 126–138.
- Kratky, O. & Porod, G. (1949) Röntgenuntersuchung geloster Fadenmoleküle. *Rec. Trav. Chim.* **68**, 1105.
- Lemma, P., Gunkel, M., Baddeley, D., *et al.* (2008) SPDM: light microscopy with single-molecule resolution at the nanoscale. *Appl. Phys. B* **93**, 1–12.
- McNally, J., Karpova, T., Cooper, J. & Conchello, J. (1999) Three-dimensional imaging by deconvolution microscopy. *Methods* **19**, 373–385.
- Munkel, C. & Langowski, J. (1998) Chromosome structure predicted by a polymer model. *Phys. Rev. E Stat. Phys. Plasmas Fluids Relat. Interdiscip. Topics* **57**, 5888–5896.
- O'Brien, T., Bult, C., Cremer, C., *et al.* (2003) Genome function and nuclear architecture: from gene expression to nanoscience. *Genome Res.* **13**, 1029–1041.
- Odenheimer, J., Kreth, G. & Heermann, D. (2005) Dynamic simulation of active/inactive chromatin domains. *J. Biol. Phys.* **31**, 351–363.
- Qu, X., Wu, D., Mets, L. & Scherer, N. (2004) Nanometer-localized multiple single-molecule fluorescence microscopy. *Proc. Natl. Acad. Sci.* **101**, 11 298–11 303.
- Rauch, J., Knoch, T., Solovei, I., *et al.* (2008) Light optical precision measurements of the active and inactive Prader-Willi syndrome imprinted regions in human cell nuclei. *Differentiation* **76–82**, 66.
- Reymann, J., Baddeley, D., Gunkel, M., *et al.* (2008) High-precision structural analysis of subnuclear complexes in fixed and live cells via spatially modulated illumination (SMI) microscopy. *Chromosome Res.* **16**, 367–382.
- Solovei, I., Cavallo, A., Schermelleh, L., *et al.* (2002) Spatial preservation of nuclear chromatin architecture during three-dimensional fluorescence in situ hybridization (3D-FISH). *Exp. Cell Res.* **276**, 10–23.
- Verschure, P. (2006) Chromosome organization and gene control: it is difficult to see the picture when you are inside the frame. *J. Cell. Biochem.* **99**, 23–34.